



ELSEVIER

Contents lists available at ScienceDirect

Ultrasonics

journal homepage: www.elsevier.com/locate/ultras

A kernel smoothing algorithm for ablation visualization in ultrasound elastography

Atul N. Ingle, Tomy Varghese*

Department of Medical Physics, University of Wisconsin School of Medicine and Public Health, Madison, WI 53705, USA

Department of Electrical and Computer Engineering, University of Wisconsin – Madison, Madison, WI 53705, USA

ARTICLE INFO

Keywords:

Ultrasound
Elastography
Ablation monitoring
Shear wave imaging
Three-dimensional reconstruction
Electrode vibration elastography

ABSTRACT

Three-dimensional visualization of tumor ablation procedures have significant clinical value because the ability to accurately visualize ablated volumes can help clinicians gauge the extent of ablated tissue necrosis and plan future treatment steps. Better control over ablation volume can prevent recurrence of tumors treated using ablative procedures. This paper presents a kernel based smoothing algorithm called MATERN SMOOTH to reconstruct shear wave velocity maps from data acquired through ultrasound electrode vibration elastography. Shear wave velocity estimates are acquired on several intersecting imaging planes that share a common axis of intersection collinear with the ablation needle. An objective method of choosing smoothing parameters from underlying data is outlined through simulations. Experimental validation was performed on data acquired from a tissue mimicking phantom. Volume estimates were found to be within 20% of the true value.

1. Introduction

Ultrasound elastography provides a non-invasive way of probing tissue stiffness and is a valuable tool for monitoring ablative treatment of cancerous tumors in the liver and other organs [1–11]. Tissue displacements are tracked using ultrasound echo data and tissue strain [5,10–12] or shear wave velocities (SWV) [2,3,9,13] are estimated from these displacements. This method provides estimates of elasticity of the tissue at specific locations in the scan plane of the ultrasound system. In this paper, a mechanical property called “shear wave velocity” is used as a quantitative surrogate for tissue stiffness because (in general) the shear wave speed is higher in stiffer tissue than softer tissue. Therefore, it provides a way to distinguish stiffer tumors from healthy tissue. An ablation procedure involves localized heating of cancerous tissue with the help of radiofrequency (RFA) or microwave ablation (MWA) modalities. Heating causes cell death and an accompanying stiffness increase which can be detected in almost real-time using ultrasound [10,14,15].

Three-dimensional (3D) reconstruction of ablated regions to determine under-treatment of tumors is a 3D problem [16–19]. 3D imaging is essential to determine if the entire tumor and surrounding margins have been successfully ablated to ensure favorable outcomes from minimally invasive procedures [20–24]. The algorithm described in this paper can be utilized with both current 3D ultrasound and

elastographic imaging performed using a wobbler [7,16,25], two-dimensional (2D) transducer arrays [26] or other innovative approaches for 3D reconstruction [25,27,28], that are utilized in this paper.

The transition from thermally necrotic tissue to healthy tissue is difficult to describe mathematically because the exact process by which cell death occurs is quite complex. The transfer of heat is governed by the bioheat transfer equation [29]. This is coupled with a model for cell death which predicts the degree of necrosis as a function of time in response to the amount of heat energy deposited in a particular area of the tissue [30]. A simplified ellipsoidal model is commonly utilized for 3D problems [31] where the shear stiffness is assumed to be a high (constant) number inside the ellipsoid and a different lower (constant) number outside the ellipsoid. In particular, for liver tissue, DeWall et al. [32] studied the behavior of stiffness as a function of distance from the ablation needle. Their mechanical testing results indicate that the stiffness can increase quite rapidly within a few millimeters of the ablation needle, but it is by no means a discontinuous jump. Therefore, sharp transitions in stiffness profiles used in simulations are an oversimplification of what is seen in practice. This paper presents a novel choice of reconstruction kernel that can capture a smooth but rapid transition of stiffness as a function of distance.

The rest of this paper is organized as follows. The experimental setup and some theoretical background related to reproducing kernel Hilbert spaces is given in Section 2 to motivate the MATERN SMOOTH

* Address at: Department of Medical Physics, 1159 WIMR, 1111 Highland Ave., Madison, WI 53705, USA.

E-mail addresses: ingle@uwalumni.com (A.N. Ingle), tvarghese@wisc.edu (T. Varghese).

<https://doi.org/10.1016/j.ultras.2018.12.006>

Received 7 March 2018; Received in revised form 10 August 2018; Accepted 12 December 2018

Available online 14 December 2018

0041-624X/ © 2018 Elsevier B.V. All rights reserved.

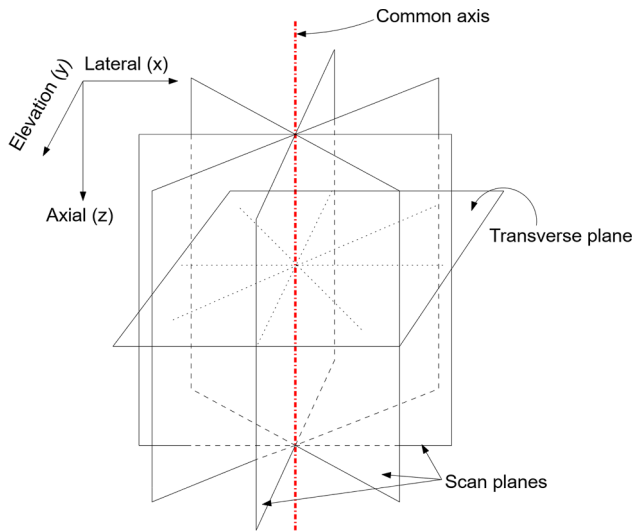


Fig. 1. The mutual orientations of different scan planes and a transverse plane are shown. The scan planes share a common axis of intersection. Each transverse plane is at a constant depth and is orthogonal to all scan planes.

algorithm. Simulation and experimental results are shown in Section 3. Some heuristics on choosing the smoothing parameters in a real world clinical setting are presented in Section 4, followed by concluding remarks in Section 5.

2. Materials and methods

2.1. Experimental setup

Radiofrequency (RF) data was acquired from an ultrasound phantom that contains a stiff region surrounded by a softer region. This arrangement mimics the presence of a stiff tumor in healthy tissue. SWV images are obtained on scanning planes that share a common axis of intersection collinear with the needle. However, this common axis is not achieved experimentally.

On account of this peculiar data acquisition arrangement also used in the clinical setting, point estimates of SWV along radial lines emanating from a common point of intersection [27] are obtained on transverse planes at constant depths. The mutual orientations of these image planes with respect to the transverse planes are shown in Fig. 1. One such transverse plane with locations of data samples is depicted in Fig. 2. Although the tumor is shown to have a perfectly circular cross-section, in reality it may be more irregularly shaped. A scatterplot of one plane of raw experimental data is shown in Fig. 3. Note that there are spurious high values of SWV close to the center where the needle is located.

The goal is to help clinicians visualize the ablated region by displaying a smooth image of the stiffness on a fine grid over the entire imaging plane while not smoothing out the boundary too much. These conflicting requirements coupled with the peculiar data sampling pattern make this problem challenging.

Note that this is fundamentally a 3D reconstruction problem. Although this study is limited to reconstruction of individual transverse planes, it may also be possible make a stack of such reconstructions to obtain a 3D view of the imaged volume, or perform a full 3D reconstruction using the complete dataset. The full 3D reconstruction approach is avoided here to keep grid size and computation time manageable. The technique presented in this paper can be easily extended by using a 3D kernel function instead of 2D. The number (P) of radial acquisition lines can be changed. Three different values of $P = 6, 12, 16$ are considered in this study.

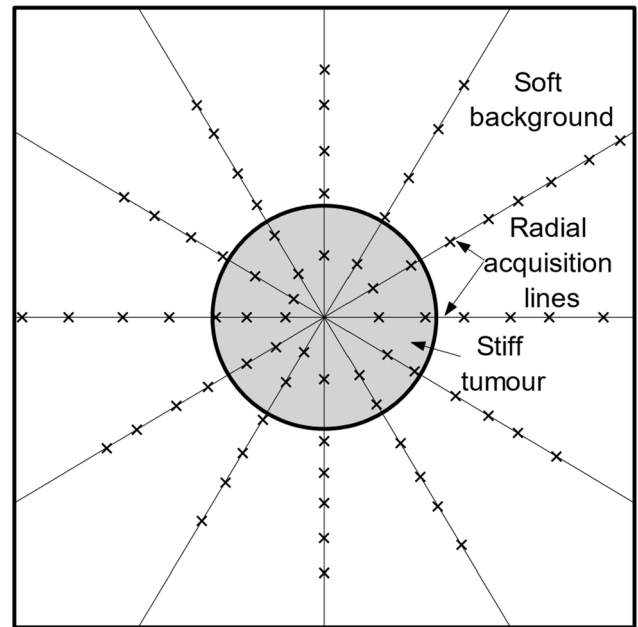


Fig. 2. Tissue stiffness measurements are available on radial intersecting lines over many transverse planes. One of the planes is shown here. Cross-marks indicate locations of data samples.

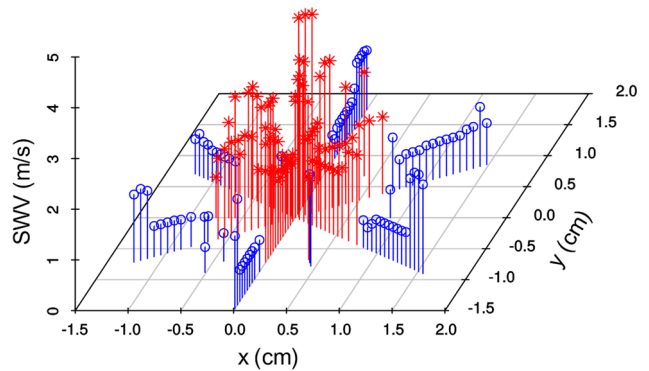


Fig. 3. Example data with 6 radial lines is shown; observe the higher peaks are closer to the origin shown in red indicating the location of the stiffer region. (For interpretation of the references to colour in this figure legend, the reader is referred to the web version of this article.)

2.2. Shear wave velocity reconstruction

SWV reconstructions are obtained for each scan plane using the time of arrival algorithm [2]. A shear wave pulse is produced by vibrating the needle using an actuator, and multiple frames of RF ultrasound data are acquired simultaneously. The scan sequence and reconstruction algorithm is discussed in more detail in the paper by DeWall et al. [9]. Displacements between consecutive frames are estimated using a one-dimensional (1D) cross-correlation algorithm and the peak displacements at each pixel are recorded to localize the shear wave pulse in space and time. The reciprocal of the slope of a plot of the time of arrival of the shear wave pulse as a function of lateral distance away from the needle is used to estimate shear wave velocity at each pixel in the scan plane [33].

2.3. Transverse plane reconstruction

Restricting attention to individual transverse planes, the SWV field can be represented by a function. $f: \mathbb{R}^2 \rightarrow [0, \infty)$. Noisy point evaluations of this function are acquired at different locations $\{t_i\}_{i=1}^P$:

$$u_i = f(t_i) + \varepsilon_i$$

where each $t_i \in \mathbb{R}^2$ is situated along the radial lines depicted in Fig. 2, and ε_i is assumed to be i.i.d. Gaussian distributed noise with unknown variance. A reconstruction of f (via interpolation or approximation) on a fine grid of M points is desired. As it stands, the problem is ill-posed because the number of data points n is usually much smaller than the size of the reconstruction grid ($n \ll M$). Typically, the number of data points obtained on each plane is on the order of 10^3 , whereas the grid may consist of 10^4 – 10^5 , points. It is necessary to restrict the space of functions that the reconstruction algorithm operates on in order to guarantee good theoretical properties:

Definition 1 ((Reproducing Kernel Hilbert Space)). A reproducing kernel Hilbert space (RKHS) \mathcal{H} of functions f on \mathbb{R}^2 is defined as the Hilbert space of functions over which the point evaluation functional is a bounded linear functional, i.e., for every $t_i \in \mathbb{R}^2$ there exists $M_i < \infty$ such that $f(t_i) \leq M_i \|f\|_{\mathcal{H}}$ for all f and $\|f\|_{\mathcal{H}}$ denotes the RKHS norm.

In the most general setting, the function f is assumed to be a member of a reproducing kernel Hilbert space (RKHS) \mathcal{H}_R with the reproducing kernel R . So the optimization problem of interest is [34]:

$$f(t) = \arg \min_{f \in \mathcal{H}_R} \sum_{i=1}^n (u_i - f(t_i))^2 + \lambda \|f\|_{\mathcal{H}_R}^2 \tag{1}$$

where $\|\cdot\|_{\mathcal{H}_R}$ denotes the RKHS norm. Another interpretation is to consider this as a regularized solution to an ill-posed inverse problem also called the Fredholm equation of the first kind, with the point evaluation function playing the role of the “blurring function” [35] in this case. The following theorem characterizes the existence of a solution to this optimization problem:

Theorem 1 ((Representer Theorem)). The solution of Eq. (1) can be expressed in the form:

$$f_{\lambda}(t) = \sum_{i=1}^n c_i R(t, t_i).$$

A short proof is presented in Appendix A. In fact, the values of c_i can be evaluated in closed form [36,37]. This theorem has important practical ramifications because it reduces the problem of finding f in an infinite dimensional Hilbert space to a problem of finding coefficients $\{c_i\}_{i=1}^n$ which is a finite dimensional problem. The smoothing parameter λ is chosen through generalized cross-validation (GCV) [37].

The choice of the kernel function R is important because it dictates the smoothness properties of the final fit. The Matérn radial basis function is used in this paper. It is defined in [38] (ch. 2, sec. 2.7), and in [39] as:

$$R(\|t - t_i\|) = \frac{\sqrt{\pi}}{2^{\nu-1}\Gamma(\nu + 1/2)r^{2\nu}} \left(\frac{\|t - t_i\|}{r}\right)^{\nu} K_{\nu}\left(\frac{\|t - t_i\|}{r}\right) \tag{2}$$

with $\nu, r > 0$, and K_{ν} is the modified Bessel function of the second kind. The unknown function can be approximated as:

$$\hat{f}(t) = \sum_{i=1}^n c_i R(\|t - t_i\|).$$

Intuitively, this formulation suggests that each data point t_i imposes a “region of influence” that varies with its distance from an arbitrary point t . Note that the absolute locations of the points t and t_i are immaterial, only the distance plays a role in the evaluation of the kernel. The characteristics of this region of influence depend on the shape of R , which is controlled using the two parameters ν and r . The smoothness (differentiability) is controlled using ν whereas the range of influence is controlled by r . It is customary to call ν the smoothness parameter whereas r is called the range (or scale) parameter of the Matérn covariance function. In particular, as $\nu \rightarrow \infty$, the Matérn Kernel converges

to an infinitely differentiable Gaussian kernel function. The advantage of using the Matérn kernel is that it provides sharper roll-offs than the infinitely differentiable Gaussian function, giving the ability preserve boundary details. The Matérn kernel is also suited to sparse data sets and more efficient than a similar Gaussian kernel. A common choice is to set $\nu = m + \frac{1}{2}$ for different non-negative integers m , resulting in a simple closed form expression for the radial basis function $R(\cdot)$ [38].

It can be shown that linear combinations of the Matérn kernel function produce functions whose frequency response decays like a polynomial [40], where the rate of decay is related to the ν parameter. The space of such functions is known as a Sobolev space, formally defined as follows ([41], Ch. 8):

Definition 2 ((Sobolev Space of functions on \mathbb{R}^2)). The Sobolev space $\mathcal{W}_{s,2}^{\alpha}(\mathbb{R}^2)$ is defined as the space of square integrable function f on \mathbb{R}^2 that satisfy

$$\int_{\mathbb{R}^2} (\alpha^2 + \omega_1^2 + \omega_2^2)^s |(Ff)(\omega_1, \omega_2)|^2 d\omega_1 d\omega_2 < \infty \tag{3}$$

where

$$(Ff)(\omega_1, \omega_2) = \int_{\mathbb{R}^2} f(x_1, x_2) e^{-j(\omega_1 x_1 + \omega_2 x_2)} dx_1 dx_2$$

denotes the 2D Fourier transform of f .

Furthermore, it can be shown that $\mathcal{W}_{s,2}^{\alpha}$ is an RKHS with the Matérn function as its reproducing kernel and hence the RKHS norm can be defined using the integral in Eq. (3).

Theorem 2. Let $R(\cdot)$ be as defined in Eq. (2). Then $\frac{\Gamma(\nu+1/2)}{4\pi^{3/2}\Gamma(\nu+1)}R(\cdot)$ is the reproducing kernel for $\mathcal{W}_{(\nu+1),2}^{1/r}(\mathbb{R}^2)$.

The proof involves some algebra to calculate the inverse 2D Fourier transform of $(\omega_1^2 + \omega_2^2)^{-\nu-1}$ as shown in Appendix B. Note that different authors set the leading normalization constants in different ways. For simulations and data analysis in presented this paper, the leading constant C was chosen in such a way that $C(d/r)^{\nu}K_{\nu}(d/r)$ is normalized to 1 when $d = 0$ for fixed (ν, r) . This choice is made possible by the fact that $K_{\nu}(u)$ behaves like $2^{\nu-1}\Gamma(\nu)u^{-\nu}$ as $u \downarrow 0$ (see [42] Sec. 9.6.9, pp. 375).

The optimization problem described in Eq. (1) can now be solved over different spaces $\mathcal{H}_{R(\nu,r)}$ by choice of kernel parameters (ν, r) . This

Input: $\{t_i\}_{i=1}^n$: data point locations in \mathbb{R}^2
 $\{y_i\}_{i=1}^n$: corresponding noisy data points
 \mathcal{S}_1 : finite set of smoothness values
 \mathcal{S}_2 : finite set of scale (range) values
Output: $f^*(\cdot)$: smooth function fit to the noisy data
 R^* : Matérn kernel for the space that f^* belongs to
 λ^* : smoothing parameter chosen using GCV

```

1: procedure MATÉRNSMOOTH( $\{t_i\}_{i=1}^n, \{y_i\}_{i=1}^n, \mathcal{S}_1, \mathcal{S}_2$ )
2:    $V^* \leftarrow \infty$ 
3:   for each  $(\nu, r) \in \mathcal{S}_1 \times \mathcal{S}_2$  do
4:      $\lambda_{GCV} \leftarrow$  smoothing parameter chosen using GCV
5:      $V \leftarrow$  GCV score at  $\lambda_{GCV}$ 
6:      $[\Sigma]_{ij} \leftarrow R_{(\nu,r)}(\|t_i - t_j\|)$ 
7:      $\mathbf{c} \leftarrow (\Sigma + \lambda_{GCV}\mathbf{I})^{-1}\mathbf{y}$ 
8:     if  $V \leq V^*$  then
9:        $V^* \leftarrow V$ 
10:       $f^*(\cdot) \leftarrow \sum_{i=1}^n c_i R_{(\nu,r)}(\|\cdot - t_i\|)$ 
11:       $R^* \leftarrow R_{(\nu,r)}$ 
12:       $\lambda^* \leftarrow \lambda_{GCV}$ 
13:    end if
14:  end for
15:  return  $(f, R^*, \lambda^*)$ 
16: end procedure

```

Fig. 4. Matérn kernel based reconstruction algorithm.

is main idea behind the MATÉRN SMOOTH algorithm presented in Fig. 4. For a fixed pair of kernel parameters, choosing the smoothing parameter λ through GCV has the following desirable theoretical property:

Theorem 3 (GCV Theorem). Let f_λ be the solution of the optimization problem in Eq. (1) and define the predictive mean squared error (PMSE) as $PMSE_n(\lambda) = \frac{1}{n} \sum_{i=1}^n (f_\lambda(t_i) - f(t_i))^2$. Let λ_{opt} be the optimal value of the smoothing parameter (that depends on the unknown function f) that minimizes the PMSE and let λ_{GCV} be the value chosen using generalized crossvalidation. Also, define the inefficiency function $I(n) = \frac{PMSE_n(\lambda_{GCV})}{PMSE_n(\lambda_{opt})}$. Then as the number of data points $n \uparrow \infty$, $I(n) \downarrow 1$.

A proof of this theorem can be found in the paper by Utreras [43] and will not be reproduced here.

Corollary 4. Let the hypotheses of Theorem 2 hold. Then the algorithm in Fig. 4, has the property that as $n \uparrow \infty$, $I(n) \downarrow 1$ on the union of Sobolev spaces $\bigcup_{(\nu,r) \in S_1 \times S_2} \mathcal{W}_{\nu,2}^r$.

The corollary is proved in Appendix C.

For comparison, a standard nearest neighbor interpolation algorithm is used to interpolate the scattered 2D data on each transverse plane. Various image quality metrics including signal-to-noise ratio (SNR), contrast (C) and contrast-to-noise ratios (CNR) are calculated using regions of interest (ROI) chosen in the inclusion and the background.

2.4. Simulation method

The following function definition was used for generating simulated 3D data:

$$g(x, y, z) = \begin{cases} 4 & \text{if } x^2 + y^2 + \frac{(z-2.25)^2}{1.5^2} \leq 1 \\ 1 & \text{otherwise.} \end{cases}$$

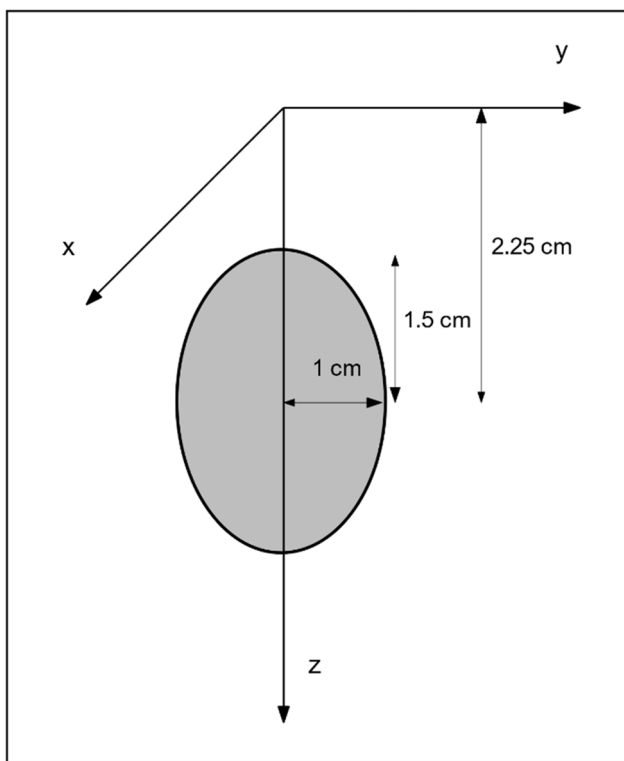


Fig. 5. Function model used for generating simulated data. The stiffer region is shaded gray and is surrounded by a softer region. The dimensions match the design of an actual phantom that is used for experimental evaluation of the algorithm.

This mimics a stiff inclusion in a soft background with a stiffness ratio of 4, with the center of the inclusion at a depth of 2.25 cm below the surface of the phantom as shown in Fig. 5. Data was generated at different depths z and the reconstruction algorithm was applied over each plane at constant depth.

To guide the selection of kernel parameters, this data generator was used to simulate noisy data with a radial acquisition pattern as shown in Fig. 2. Three different cases for $P = 6, 12, 16$ using angular increments of π/P , 100 radial samples over 4 cm and 100 samples over a depth of 4.5 cm in the z direction were used. The reconstruction was performed in the bounded box $[-2,2] \times [-2,2] \times [0,4.5]$. Zero mean additive Gaussian noise with a standard deviation of $\sigma = 0.5$ was used, and the simulation was run 10 times for each pair of (ν, r) values, with $\nu \in \{0.2, 0.9, 1.5, 2.5\}$ and $r \in \{0.04, 0.1, 0.2, 0.4, 0.6\}$. Note that the standard deviation of 0.5 when detecting a jump of 3 units corresponds to a signal to noise ratio of approximately 15 dB which resembles the kind of noise seen in ultrasound based SWV measurements. The numerical values used in this simulation were chosen to match the ground truth that one theoretically expects to observe on a phantom with an ellipsoidal inclusion.

3. Results

3.1. Simulation results

The SWV is reconstructed on a fine grid of $M = 10^6$ points using the Matérn radial basis approximation and the predictive mean squared error is estimated using:

$$PMSE(\nu, r) = \frac{1}{M} \sum_{l,m,n} \left[\hat{g}\left(\frac{4(l-50)}{100}, \frac{4(m-50)}{100}, \frac{4.5n}{100}\right) - g\left(\frac{4(l-50)}{100}, \frac{4(m-50)}{100}, \frac{4.5n}{100}\right) \right]^2$$

where \hat{g} is the reconstructed function, g is the true function and the sum is calculated over a discrete grid of points $0 \leq l, m, n \leq 99$ and $(l, m, n) \in \mathbb{Z}^3$. Mean and standard deviation of PMSE from these Monte Carlo simulations are shown in Tables 1–3.

It is clear from these tables that the PMSE improves as the number of radial lines P increases. The pair $(\nu, r) = (0.9, 0.4)$ gives the lowest reconstruction error in all three cases. The next best choice of parameters, if first order mean squared differentiability is desired, are $(\nu, r) = (1.5, 0.4)$. This choice of kernel parameters is used later for reconstructions from experimental data acquired on a tissue mimicking phantom. It is worth noting that the reconstruction quality is more sensitive to the choice of range r than the smoothness ν . A surface plot of the PMSE over a wider range of ν and r values is shown in Fig. 6. By controlling ν and r , it is possible to reduce the spoke-wheel artifacts that appear due to the radial sampling strategy (Fig. 7).

3.2. Experimental results

Experimental data was acquired on a tissue mimicking phantom that consisted of an ellipsoidal inclusion in a soft background with known stiffness. The approximate mathematical description of the size and location of the inclusion matches the model used for generating simulated data as described in the Materials and Methods section. Three different data sets are obtained experimentally by changing the number of radial sampling lines to $P = 6, 12$ and 16 , respectively.

Fig. 8 shows the reconstructed SWV images over one particular image plane passing through the center of the inclusion. The top row of images show reconstructions using incorrectly chosen kernel parameters which result in bright streaks along the radial sampling lines. But when the optimal (ν, r) pair is used, this spokewheel artifact is greatly reduced as seen in the second row of images. Fig. 9 shows reconstruction results using additional (ν, r) combinations for $P = 6$ planes. Notice that increasing values of (ν, r) correspond to increased level of smoothing.

SWV values obtained using MATÉRN SMOOTH algorithm and nearest

Table 1
Mean and standard deviation of PMSE for P = 6 radial lines.

ν	r				
	0.04	0.1	0.2	0.4	0.6
0.2	0.920 (0.019)	0.546 (0.020)	0.284 (0.017)	0.154 (0.011)	0.126 (0.009)
0.9	0.650 (0.015)	0.276 (0.011)	0.117 (0.007)	0.085 (0.006)	0.085 (0.007)
1.5	0.551 (0.013)	0.197 (0.009)	0.092 (0.006)	0.088 (0.010)	0.099 (0.016)
2.5	0.449 (0.011)	0.136 (0.007)	0.089 (0.008)	0.149 (0.041)	0.264 (0.098)

Table 2
Mean and standard deviation of PMSE for P = 12 radial lines.

ν	r				
	0.04	0.1	0.2	0.4	0.6
0.2	0.778 (0.015)	0.341 (0.013)	0.167 (0.008)	0.108 (0.005)	0.096 (0.005)
0.9	0.420 (0.011)	0.134 (0.006)	0.084 (0.004)	0.074 (0.003)	0.074 (0.003)
1.5	0.313 (0.009)	0.102 (0.005)	0.078 (0.004)	0.078 (0.003)	0.083 (0.004)
2.5	0.221 (0.007)	0.087 (0.004)	0.080 (0.003)	0.114 (0.011)	0.167 (0.027)

Table 3
Mean and standard deviation of PMSE for P = 16 radial lines.

ν	r				
	0.04	0.1	0.2	0.4	0.6
0.2	0.688 (0.022)	0.265 (0.015)	0.135 (0.009)	0.093 (0.006)	0.084 (0.005)
0.9	0.317 (0.014)	0.107 (0.006)	0.075 (0.004)	0.068 (0.003)	0.069 (0.003)
1.5	0.223 (0.011)	0.087 (0.005)	0.072 (0.003)	0.074 (0.003)	0.082 (0.004)
2.5	0.153 (0.008)	0.079 (0.004)	0.077 (0.003)	0.128 (0.021)	0.206 (0.055)

neighbor interpolation are shown in Table 4. These values agree with SWV measurements obtained using a commercial (SuperSonic Imagine) ultrasound scanner. Table 5 shows various image quality metrics calculated using two regions of interest fixed in the background and the inclusion respectively. The kernel smoothing algorithm provides higher SNR than nearest neighbor interpolation.

Inclusion volume is an important quantity that helps clinicians gauge the extent of the ablated region and determine if additional treatment would be necessary. A clinician usually measures the principal axes of the inclusion from the reconstructed images displayed on a graphical user interface. Volume estimates for the ellipsoid are obtained from experimental reconstructions by measuring the three semi-principal axes (a, b, c) and using the ellipsoid volume formula $V = \frac{4}{3}\pi abc$. With a smoothing algorithm there is a risk of over-smoothing which can lead to loss of sharp boundary information and cause the volume to be severely under-estimated. Results for different numbers of radial lines along with the ground truth volume are shown in the box plot in Fig. 10. Note that the volume measurements using MATÉRN SMOOTH reconstruction are very similar to those obtained from a standard nearest neighbor interpolation.

The estimated volume is biased and underestimates the true volume in all three cases by about 20%. This is expected because there are multiple smoothing and noise filtering steps in the signal processing leading up to the final images shown in Fig. 8, which erodes the boundary detail. The bias in measuring the principal axes of the ellipsoid is only about 7% which gets magnified by a factor of 3 when calculating the volume. It is possible to create a thresholding procedure that converts the reconstructed images into binary images that are white inside the inclusion and black outside. The clinician can control a slider to smoothly transition between different levels of thresholding and obtain images like Fig. 11.

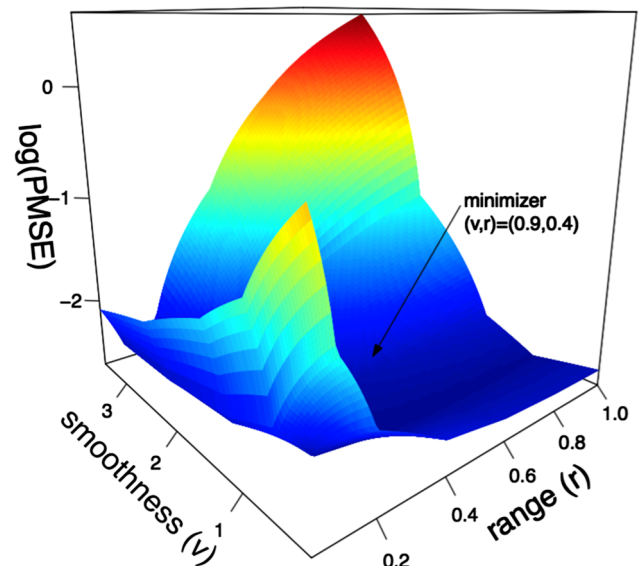


Fig. 6. A surface plot of PMSE values for different combinations of (ν, r) is shown. The local minimizer is also shown. For every pair of values, the tuning parameter λ was chosen through GCV.

4. Discussion

The Matérn kernel reconstruction algorithm developed in this paper provides an objective method for choosing the degree of smoothness for 3D reconstructions from a stack of 2D planes. For computational complexity reasons, this paper presented an algorithm which uses an intermediate step of reconstructing 2D planes and stacking them to form a 3D reconstruction. It is possible to generate the 3D

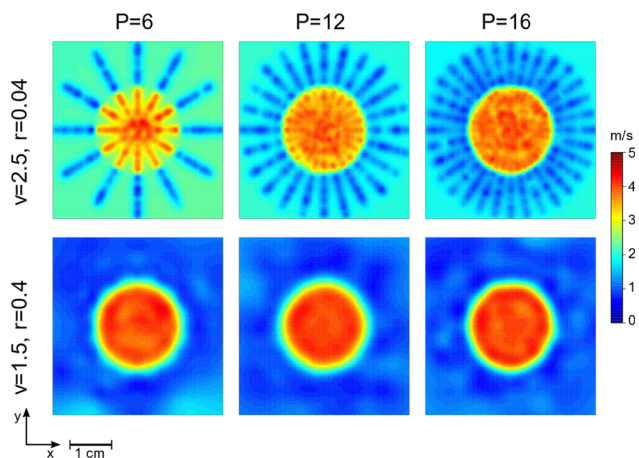


Fig. 7. Reconstructions from simulated data using different Matérn kernel parameters for different numbers of radial lines of data. Top row shows the spoke-wheel image artifact which can be avoided by proper choice of (ν, r) as seen in the bottom row. Top row $(\nu, r) = (2.5, 0.04)$ and bottom row $(\nu, r) = (1.5, 0.4)$.

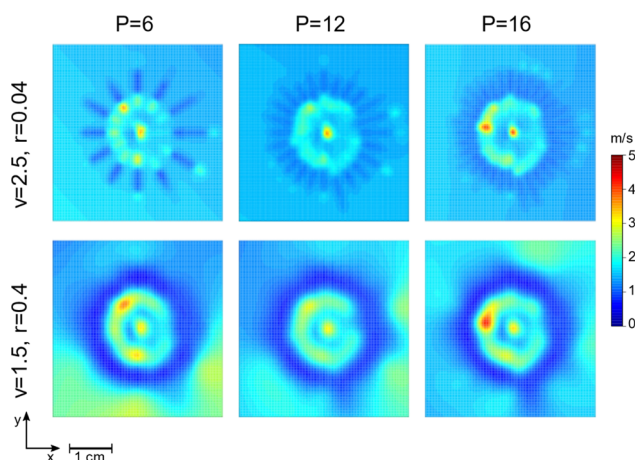


Fig. 8. Reconstructions of experimental data using different Matérn kernel parameters for different numbers of radial lines of data. Top row shows that the spoke-wheel image artifact is ameliorated using $(\nu, r) = (1.5, 0.4)$ as seen in the bottom row. Top row $(\nu, r) = (2.5, 0.04)$ and bottom row $(\nu, r) = (1.5, 0.4)$.

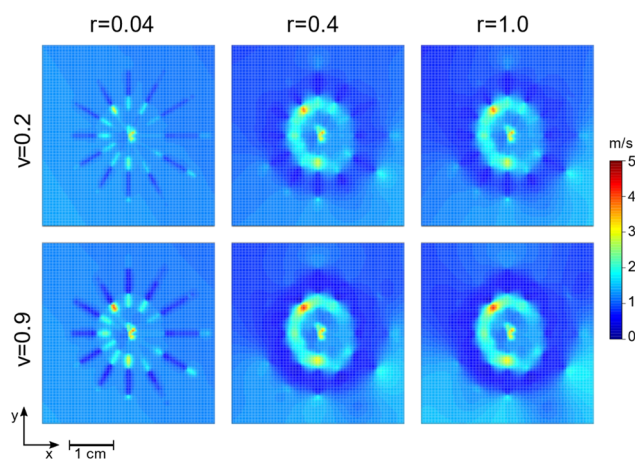


Fig. 9. Reconstructions of experimental data using different Matérn kernel parameters for different (ν, r) combinations. Top row $\nu = 0.2$, bottom row $\nu = 0.9$, columns left-to-right, $r = 0.04, 0.4, 1.0$.

Table 4

SWV values (m/s) using the MATÉRN SMOOTH algorithm and nearest neighbor interpolation for comparison in the inclusion (inc) and background (bkg) regions. SWV values were also measured using a commercial SuperSonic Imagine ultrasound scanner were estimated to be 0.9 (0.07) m/s in the inclusion and 1.2 (0.03) m/s in the background. Numbers in parantheses indicate one standard deviation.

	MATÉRN SMOOTH algorithm		Nearest neighbor interpolation	
	inc	bkg	inc	bkg
P = 6	1.44 (0.29)	0.83 (0.13)	1.48 (0.40)	0.88 (0.20)
P = 12	1.49 (0.37)	0.89 (0.20)	1.51 (0.47)	0.94 (0.23)
P = 16	1.77 (1.12)	0.90 (0.23)	1.64 (0.86)	0.97 (0.24)

Table 5

Image quality metrics SNR, C and CNR in dB.

	MATÉRN SMOOTH algorithm				Nearest neighbor interpolation			
	SNR (inc)	SNR (bkg)	C	CNR	SNR (inc)	SNR (bkg)	C	CNR
P = 6	13.8	16.1	4.8	5.5	11.6	12.9	4.5	2
P = 12	12.1	13.0	4.5	3.1	10.3	12.1	4.1	0.6

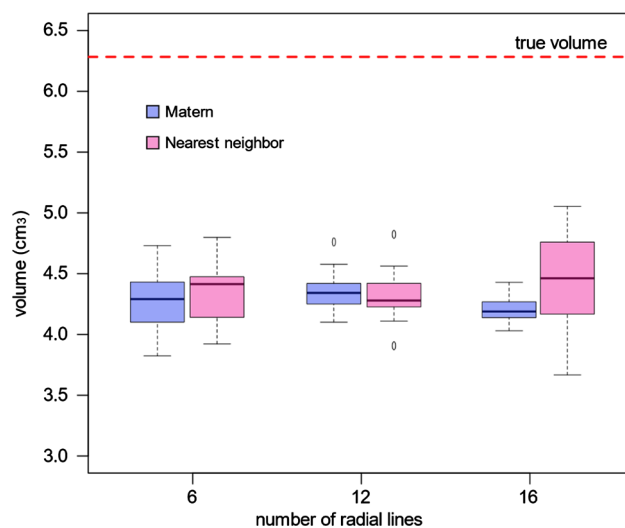


Fig. 10. Box plot showing the volume estimates when the ellipsoidal inclusion is reconstructed using 6, 12, 16 radial acquisition lines. The true volume is shown using the constant horizontal line.

reconstruction directly by treating the SWV values as a function of 3D coordinates. This has practical significance because the process of ablation is governed by a complex coupled system of heat transfer and tissue necrosis, that may be difficult to model accurately [44]. The algorithm presented in Fig. 4 has good theoretical properties in that it applies an optimum amount of smoothing by careful choice of the smoothing parameter and the kernel function. The final output will be sensitive to the choice of the sets S_1 and S_2 . Although it is difficult to develop a general theory on choosing these sets, some heuristic guidelines are given below.

By inspecting the B-mode and SWV image of the ablated area, the clinician can get an idea of the sharpness of the transition from ablated region to healthy tissue. Their subjective judgment can be used to guess some reasonable range of integer values for degree of smoothness for the transition and choosing $\nu = m + \frac{1}{2}$ for small integer values of m . Additionally, if the B-mode or SWV image suggests any discontinuities, values of $\nu < 0.5$ that will promote even sharper, non-differentiable

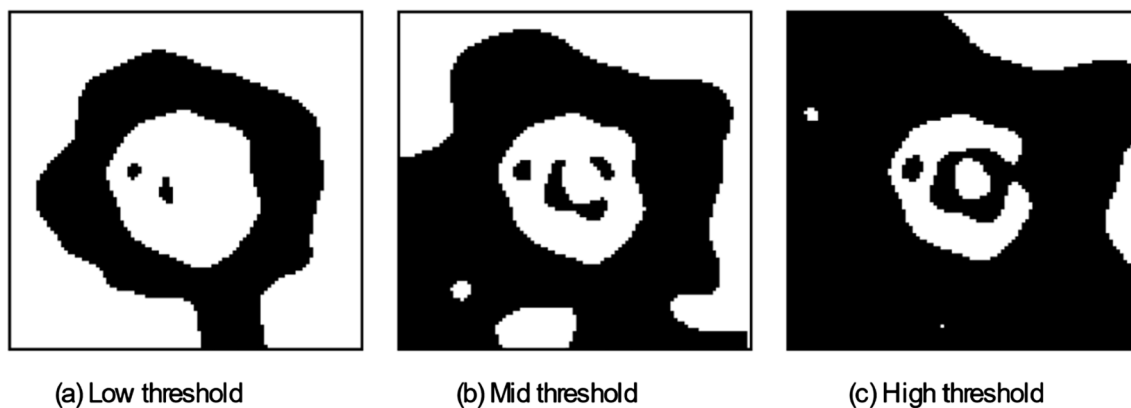


Fig. 11. Thresholded images created from the $P = 16$ image from the bottom right image in Fig. 8. As the threshold is gradually increased, a smaller region of the image appears as an inclusion.

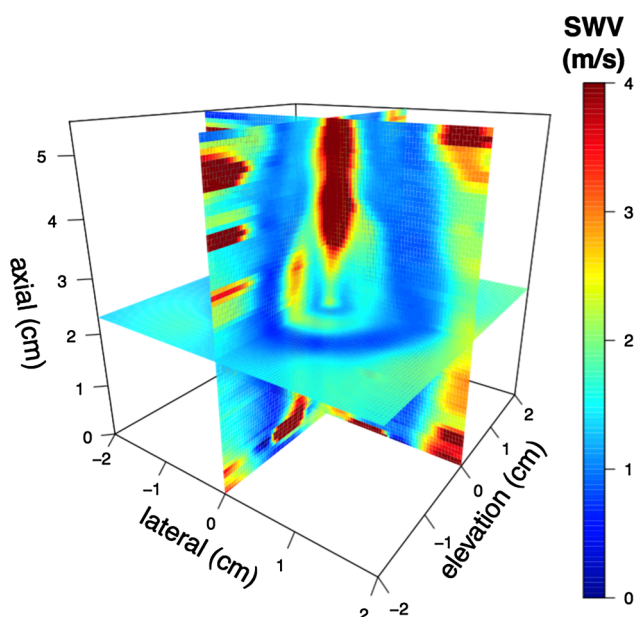


Fig. 12. A 3D rendering of the stiffer inclusion phantom produced from a stack of individual 2D planes at different depths.

reconstructions may be used. Unlike ν which has an intuitive relationship to the smoothness of the final fit, the choice of scale parameter r is subtler. As a rule of thumb, r should be large enough so that more than one neighboring data point is captured by a kernel centered around any data point, and should not be so large that far away points are unnecessarily weighted heavily.

Different values of r corresponding to the k^{th} smallest distance between any two data points can be tried for, say, $k = 1, 2, 3, \dots$, and using the simulation method discussed previously, the combination of values that provide a local minimum value of (ν, r) should be used.

Various artifacts are visible in the final 3D visualization shown in Fig. 12. There is a high SWV artifact close to the needle due to the presence of specular reflections from the needle in that region. Next, a low velocity artifact can be seen inside the ellipsoid because the shear

Appendix A: Proof of Theorem 1

Define the space $\mathcal{H}_0 = \{f \in \mathcal{H}_R: f = \sum_{i=1}^n a_i R(t, t_i)\}$. Clearly \mathcal{H}_0 is a subspace of \mathcal{H}_R and one can write $\mathcal{H}_R = \mathcal{H}_0 \oplus \mathcal{H}_1$, where \mathcal{H}_1 consists of all the functions that are orthogonal to the functions in the subspace \mathcal{H}_0 . So, any $g \in \mathcal{H}_R$ can be represented as $g = g_0 + g_1$ such that $\|g_0 + g_1\|_{\mathcal{H}_R}^2 = \|g_0\|_{\mathcal{H}_R}^2 + \|g_1\|_{\mathcal{H}_R}^2$. Moreover, $g(t_i) = g_0(t_i)$ because point evaluation at t_i is equivalent to an inner product operation with the reproducing kernel $R(\cdot, t_i) \in \mathcal{H}_0$. This implies that:

wave does not instantaneously start traveling at its maximum speed in the stiff medium after originating from the line source (ablation needle). The high velocity artifacts close to the edge of the volume can be attributed to lower lateral resolution from reduction in effective aperture size near the edge of the transducer.

The ability to obtain real-time volumetric visualization of the ablated region is of paramount interest in the clinic after the ablation procedure is completed. Approaches that can perform reconstructions with sparse data for faster and accurate visualizations are therefore important. In addition, thermal ablation regions created with RFA or MWA are generally ellipsoidal and therefore the circular approximation used does not introduce significant errors.

5. Conclusion

The Matérn kernel smoothing algorithm provides a flexible yet objective way of reducing the spoke-wheel artifacts in SWV maps reconstructed from noisy ultrasound elastography data. The predictive mean squared error from a known simulation model was used for making an educated guess for kernel parameters. In phantom data, the volume was underestimated by about 20% because of loss in boundary detail from smoothing. The number of radial acquisition lines used in reconstruction did not make much difference to the choice of kernel parameters. This is probably because the inclusion shape is perfectly symmetric (ellipsoidal) and the planar cross-sections are circular. Increasing the number of radial acquisition lines will be advantageous if the boundary is more undulating, or has corners. A final thresholding step can be used to automate the process of manually annotating ablation boundaries for size estimation.

Acknowledgements

This work was supported in part by the National Institutes of Health National Cancer Institute (NIH-NCI) grant R01CA112192. The authors would like to thank Prof. Grace Wahba, Ph.D for discussions about reproducing kernel Hilbert spaces and for suggesting the use of Matérn kernel for the reconstruction problem presented in this paper and Prof. Christopher Brace, Ph.D for helpful discussions about the physics of ablation and tissue necrosis.

$$\begin{aligned} \frac{1}{n} \sum_{i=1}^n (u_i - g(t_i))^2 + \lambda \|g\|_{\mathcal{H}_R}^2 &= \frac{1}{n} \sum_{i=1}^n (u_i - g_0(t_i))^2 + \lambda (\|g_0\|_{\mathcal{H}_R}^2 + \|g_1\|_{\mathcal{H}_R}^2) \\ &\geq \frac{1}{n} \sum_{i=1}^n (u_i - g_0(t_i))^2 + \lambda \|g_0\|_{\mathcal{H}_R}^2 \end{aligned}$$

so that the solution must lie in \mathcal{H}_0 . The solution is unique because the objective function in Eq. (1) is convex and coercive.

Appendix B.: Proof of Theorem 2

By definition of the Gamma function,

$$\Gamma(\nu + 1) = \int_0^\infty u^\nu e^{-u} du$$

where, substituting $u = (1/r^2 + \omega_1^2 + \omega_2^2)$ and rearrangement yields:

$$(1/r^2 + \omega_1^2 + \omega_2^2)^{-\nu-1} = \frac{1}{\Gamma(\nu + 1)} \int_0^\infty t^\nu e^{-t(1/r^2 + \omega_1^2 + \omega_2^2)} dt \tag{B.1}$$

The inverse 2D Fourier transform is given by:

$$\frac{1}{(2\pi)^2} \int_{\mathbb{R}^2} \frac{e^{j(\omega_1 x_1 + \omega_2 x_2)}}{(1/r^2 + \omega_1^2 + \omega_2^2)^{\nu+1}} d\omega_1 d\omega_2 \tag{B.2}$$

$$= \frac{1}{(2\pi)^2 \Gamma(\nu + 1)} \int_{t=0}^\infty t^\nu e^{-t/r^2} \int_{\mathbb{R}^2} \frac{e^{-t(\omega_1^2 + \omega_2^2)} e^{j(\omega_1 x_1 + \omega_2 x_2)}}{(1/r^2 + \omega_1^2 + \omega_2^2)^{\nu+1}} d\omega_1 d\omega_2 dt \tag{B.3}$$

$$= \frac{1}{(2\pi)^2 \Gamma(\nu + 1)} \int_{t=0}^\infty t^\nu e^{-\frac{t}{r^2} - \frac{x_1^2 + x_2^2}{4t}} \int_{\mathbb{R}^2} \frac{e^{-t\left(\left(\omega_1 - j\frac{x_1}{2t}\right)^2 + \left(\omega_2 - j\frac{x_2}{2t}\right)^2\right)}}{(1/r^2 + \omega_1^2 + \omega_2^2)^{\nu+1}} d\omega_1 d\omega_2 dt \tag{B.4}$$

$$= \frac{1}{(2\pi)^2 \Gamma(\nu + 1)} \int_{t=0}^\infty t^\nu e^{-\frac{t}{r^2} - \frac{x_1^2 + x_2^2}{4t}} dt \tag{B.5}$$

$$= \frac{1}{(2\pi)^2 \Gamma(\nu + 1)} \int_{t=0}^\infty 2 \left[\frac{\sqrt{x_1^2 + x_2^2}}{2/r} \right]^\nu \cosh(uv) e^{-\frac{1}{r} \sqrt{x_1^2 + x_2^2} \cosh(u)} du \tag{B.6}$$

$$= \frac{1}{2^{\nu+1} \pi \Gamma(\nu + 1) r^{-2\nu}} \left[\frac{\sqrt{x_1^2 + x_2^2}}{2/r} \right]^\nu K_\nu \left[\frac{\sqrt{x_1^2 + x_2^2}}{r} \right] \tag{B.7}$$

$$= \frac{\Gamma\left(\nu + \frac{1}{2}\right)}{4\pi^{3/2} \Gamma(\nu + 1)} R(\|(x_1, x_2) - (0, 0)\|) \tag{B.8}$$

where Eq. (B.3) is obtained by substituting Eq. (B.1) in (B.2); Eq. (B.5) follows from the fact that the inner integral is the integral of a 2D Gaussian function which evaluates to π/t ; Eq. (B.6) is obtained by substituting $t = \frac{1}{2} r e^{-u} \sqrt{x_1^2 + x_2^2}$ and using the fact that $\cosh(u)$ is an even function; and Eq. (B.7) follows from the definition of the modified Bessel function of the second kind ([42], Sec. 9.6.24, pp. 376). Finally, Eq. (B.8) follows from the definition of $R(\cdot)$ in Eq. (2).

Appendix C.: Proof of Corollary 4

Fix any $(\nu, r) \in S_1 \times S_2$. Then from Theorem 2, as $n \uparrow \infty$, $I_{\nu,r}(n) \downarrow 1$, where the dependence of the inefficiency function on ν and r is explicitly shown. Since $R_{\nu,r}$ is the reproducing kernel for $\mathcal{W}_{(\nu+1),2}^{1/r}$, solving the optimization problem in Eq. (1) produces a function $f \in \mathcal{W}_{(\nu+1),2}^{1/r}$. Repeating this process for all (ν, r) pairs it follows from Theorem 2 that $I_{\nu,r}(n) \downarrow 1$ with $f \in \bigcup_{\nu,r} \mathcal{W}_{(\nu+1),2}^{1/r}$.

References

[1] J. Ophir, S.K. Alam, B. Garra, F. Kallel, E. Konofagou, T. Krouskop, et al., Elastography: ultrasonic estimation and imaging of the elastic properties of tissues, Proc. Inst. Mech. Eng. H 213 (1999) 203–233.
 [2] M.L. Palmeri, M.H. Wang, J.J. Dahl, K.D. Frinkley, K.R. Nightingale, Quantifying hepatic shear modulus in vivo using acoustic radiation force, Ultrasound Med. Biol. 34 (2008) 546–558.
 [3] E. Sapin-de Broses, J.L. Gennisson, M. Pernot, M. Fink, M. Tanter, Temperature dependence of the shear modulus of soft tissues assessed by ultrasound, Phys. Med. Biol. 55 (2010) 1701–1718.
 [4] Z. Zhou, W. Wu, S. Wu, J. Xia, C.Y. Wang, C. Yang, et al., A survey of ultrasound elastography approaches to percutaneous ablation monitoring, Proc. Inst. Mech. Eng. H 228 (2014) 1069–1082.
 [5] T. Varghese, Quasi-static ultrasound elastography, Ultrasound Clin. 4 (Jul 2009) 323–338.

[6] M. Zhang, B. Castaneda, J. Christensen, W.E. Saad, K. Bylund, K. Hoyt, et al., Real-time sonoelastography of hepatic thermal lesions in a swine model, Med. Phys. 35 (2008) 4132–4141.
 [7] H. Rivaz, I. Fleming, L. Assumpcao, G. Fichtinger, U.M. Hamper, M.A. Choti, et al., Ablation monitoring with elastography: 2D in-vivo and 3D ex-vivo studies, Med. Image Comput. Assist. Interv. 11 (2008) 458–466.
 [8] W. Yang, T. Ziemlewicz, T. Varghese, M. Alexander, N. Rubert, A.N. Ingle, et al., Post-procedure evaluation of microwave ablations of hepatocellular carcinomas using electrode displacement elastography, Ultrasound Med. Biol. 42 (2016) 2893–2902.
 [9] R.J. DeWall, T. Varghese, E.L. Madsen, Shear wave velocity imaging using transient electrode perturbation: phantom and ex vivo validation, IEEE Trans. Med. Imaging 30 (Mar 2011) 666–678.
 [10] T. Varghese, J.A. Zagzebski, F.T. Lee Jr., Elastographic imaging of thermal lesions in the liver in vivo following radiofrequency ablation: preliminary results, Ultrasound Med. Biol. 28 (2002) 1467–1473 Nov–Dec.
 [11] R. Ahmed, R. Arfin, M.H. Rubel, K.K. Islam, C. Jia, D. Metaxas, et al., Comparison of

- windowing effects on elastography images: simulation phantom and in vivo studies, *Ultrasonics* 66 (2016) 140–153.
- [12] J. Ophir, F. Kallel, T. Varghese, M. Bertrand, I. Cespedes, H. Ponnekanti, Elastography: a systems approach, *Int. J. Imaging Syst. Technol.* 8 (1997) 89–103.
- [13] A. Ingle, C. Ma, T. Varghese, Ultrasonic tracking of shear waves using a particle filter, *Med. Phys.* 42 (2015) 6711–6724.
- [14] S. Bharat, U. Techavipoo, M.Z. Kiss, W. Liu, T. Varghese, Monitoring stiffness changes in lesions after radiofrequency ablation at different temperatures and durations of ablation, *Ultrasound Med. Biol.* 31 (Mar 2005) 415–422.
- [15] W. Yang, T. Varghese, T. Ziemlewicz, M. Alexander, M.G. Lubner, J.L. Hinshaw, et al., Delineation of post-procedure ablation regions with electrode displacement elastography with a comparison to acoustic radiation force impulse imaging, *Ultrasound Med. Biol.* 43 (2017) 1953–1962.
- [16] S. Bharat, T.G. Fisher, T. Varghese, T.J. Hall, J. Jiang, E.L. Madsen, et al., Three-dimensional electrode displacement elastography using the Siemens C7F2 fourSight four-dimensional ultrasound transducer, *Ultrasound Med. Biol.* 34 (Aug 2008) 1307–1316.
- [17] H. Neshat, D.W. Cool, K. Barker, L. Gardi, N. Kakani, A. Fenster, A 3D ultrasound scanning system for image guided liver interventions, *Med. Phys.* 40 (2013) 112903.
- [18] J. Xu, Z.Z. Jia, Z.J. Song, X.D. Yang, K. Chen, P. Liang, Three-dimensional ultrasound image-guided robotic system for accurate microwave coagulation of malignant liver tumours, *Int. J. Med. Robot* 6 (2010) 256–268.
- [19] C. Papadacci, E.A. Bunting, E.E. Konofagou, 3D quasi-static ultrasound elastography with plane wave in vivo, *IEEE Trans. Med. Imaging* 36 (2017) 357–365.
- [20] T.A. Potretzke, T.J. Ziemlewicz, J.L. Hinshaw, M.G. Lubner, S.A. Wells, C.L. Brace, et al., Microwave versus radiofrequency ablation treatment for hepatocellular carcinoma: a comparison of efficacy at a single center, *J. Vasc. Interv. Radiol.* 27 (2016) 631–638.
- [21] T.J. Ziemlewicz, J.L. Hinshaw, M.G. Lubner, C.L. Brace, M.L. Alexander, P. Agarwal, et al., Percutaneous microwave ablation of hepatocellular carcinoma with a gas-cooled system: initial clinical results with 107 tumors, *J. Vasc. Interv. Radiol.* 26 (Jan 2015) 62–68.
- [22] R. Lencioni, L. Crocetti, Local-regional treatment of hepatocellular carcinoma, *Radiology* 262 (Jan 2012) 43–58.
- [23] P. Liang, Y. Wang, Microwave ablation of hepatocellular carcinoma, *Oncology* 72 (Suppl 1) (2007) 124–131.
- [24] M. Maluccio, A. Covey, Recent progress in understanding, diagnosing, and treating hepatocellular carcinoma, *CA Cancer J. Clin.* 62 (2012) 394–399 Nov–Dec.
- [25] W. Yang, A. Ingle, T. Varghese, Comparison of three dimensional strain volume reconstructions using SOUPR and wobbler based acquisitions: a phantom study, *Med. Phys.* 43 (2016) 1615–1626.
- [26] C. Papadacci, E. Bunting, E. Konofagou, 3D quasi-static ultrasound elastography with plane wave in vivo, *IEEE Trans. Med. Imaging* (2016) (in press).
- [27] A. Ingle, T. Varghese, Three-dimensional sheaf of ultrasound planes reconstruction (SOUPR) of ablated volumes, *IEEE Trans. Med. Imag.* 33 (Aug 2014) 1677–1688.
- [28] A. Ingle, T. Varghese, W. Sethares, Efficient 3D reconstruction in ultrasound elastography via a sparse iteration based on markov random fields, *IEEE Trans. Ultrason. Ferroel. Freq. Cont.* 64 (2017) 491–499.
- [29] J. Chiang, P. Wang, C.L. Brace, Computational modelling of microwave tumour ablations, *Int. J. Hyperthermia* 29 (2013) 308–317.
- [30] A.S. Wright, D.M. Mahvi, D.G. Haemmerich, F.T.J. Lee, Minimally invasive approaches in management of hepatic tumors, *Surg. Technol. Int.* 11 (2003) 144–153.
- [31] R.S. Lazebnik, B.D. Weinberg, M.S. Breen, J.S. Lewin, D.L. Wilson, Semiautomatic parametric model-based 3D lesion segmentation for evaluation of MR-guided radiofrequency ablation therapy, *Acad. Radiol.* 12 (2005) 1491–1501.
- [32] R.J. DeWall, T. Varghese, C.L. Brace, Quantifying local stiffness variations in radiofrequency ablations with dynamic indentation, *IEEE Trans. Biomed. Eng.* 59 (Mar 2012) 728–735.
- [33] A. Ingle, J. Bucklew, W. Sethares, T. Varghese, Slope estimation in noisy piecewise linear functions, *Signal Process.* 108 (2015) 576–588.
- [34] J. Carew, R. Dalal, G. Wahba, S. Fain, A nonparametric method for estimation of arterial wall shear stress, *Proceedings of International Society of Magnetic Resonance in Medicine (ISMRM)*, 2004, p. 1924.
- [35] G. Wahba, Y. Wang, When is the optimal regularization parameter insensitive to the choice of the loss function? *Commun. Stat. – Theory Methods* 19 (1990) 1685–1700.
- [36] G. Kimeldorf, G. Wahba, Some results on Tchebycheffian spline functions, *J. Math. Anal. Appl.* 33 (1971) 82–95.
- [37] G. Wahba, *Spline Models for Observational Data*, Society for Industrial and Applied Mathematics, Philadelphia, PA, 1990 CBMS-NSF Regional Conference Series in Applied Mathematics.
- [38] M.L. Stein, *Interpolation of Spatial Data Some Theory for Kriging*, Springer-Verlag, New York, 1999.
- [39] B. Minasny, A.B. McBratney, The matern function as a general model for soil variograms, presented at the Conference: 5th International Conference on Pedometrics Univ Reading UK, 2005.
- [40] S. Ramani, D. Van De Ville, T. Blu, M. Unser, Nonideal sampling and regularization theory, *IEEE Trans. Sig. Proc.* 56 (2008) 1055–1070.
- [41] R.S. Strichartz, *A guide to distribution theory and Fourier transforms*, World Scientific Publishing Company, Singapore, 2003.
- [42] M. Abramowitz, I.A. Stegun, *Handbook of Mathematical Functions with Formulas, Graphs, and Mathematical Tables*, Dover Publications, Dover, UK, 1964.
- [43] F. Utreras, On generalized cross-validation for multivariate smoothing spline functions, *SIAM J. Scientific Stat. Computing* 8 (1987) 630–643.
- [44] D. Yang, M.C. Converse, D.M. Mahvi, J.G. Webster, Measurement and analysis of tissue temperature during microwave liver ablation, *IEEE Trans. Biomed. Eng.* 54 (2007) 150–155.